NANO LETTERS

Letter

pubs.acs.org/NanoLett

Interfacial Oxygen Stabilizes Composite Silicon Anodes

Chuan-Fu Sun,[†] Hongli Zhu,[‡] Morihiro Okada,[†,§] Karen Gaskell,[†] Yoku Inoue,[∥] Liangbing Hu,[‡] and YuHuang Wang*,[†]

[†]Department of Chemistry and Biochemistry, University of Maryland, College Park, Maryland 20742, United States

[‡]Department of Materials Science and Engineering, University of Maryland, College Park, Maryland 20742, United States

[§]Research Institute of Electronics, Shizuoka University, 3-5-1 Johoku, Hamamatsu 432-8011, Japan

[∥]Department of Electronics and Materials Science, Shizuoka University, 3-5-1 Johoku, Hamamatsu 432-8561, Japan

Supporting Information

ABSTRACT: Silicon can store Li^+ at a capacity 10 times that of graphite anodes. However, to harness this remarkable potential for electrical energy storage, one has to address the multifaceted challenge of volume change inherent to high capacity electrode materials. Here, we show that, solely by chemical tailoring of Si-carbon interface with atomic oxygen, the cycle life of Si/carbon matrix-composite electrodes can be substantially improved, by 300%, even at high mass loadings. The interface tailored electrodes simultaneously attain high areal capacity (3.86 mAh/cm^2), high specific capacity (922 mAh/g based on the mass of the entire electrode), and excellent cyclability (80% retention of capacity after 160 cycles), which are among the highest reported. Even at a high rate of 1C, the areal capacity approaches 1.61 mAh/cm^2 at the 500th cycle. This remarkable electrochemical performance is directly correlated with significantly improved structural and electrical interconnections throughout the entire electrode due to chemical tailoring of the Si-carbon interface with atomic oxygen. Our results demonstrate that interfacial bonding, a new dimension that has yet to be explored, can play an unexpectedly important role in addressing the multifaceted challenge of Si anodes.

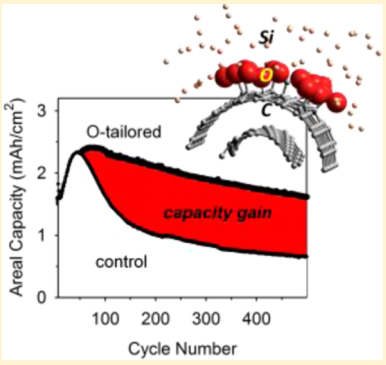

KEYWORDS: *electrical energy storage, nanocomposite, high-capacity electrode, interfacial chemistry, lithium ion battery, silicon anode*

High-capacity electrode materials are inherently accompanied by large volume changes that pose a significant, multifaceted challenge to their functions in rechargeable batteries.[1−3] At the apex of this challenge is silicon, which has a theoretical capacity as high as 3579 mAh/g at room temperature, ∼10 times that of graphite anodes used in lithium ion batteries.[4,5] However, the large volume change (∼270%) during lithium ion insertion/extraction induces enormous mechanical strain that causes pulverization of Si, loss of electrical contact, and uncontrolled growth of solid electrolyte interphase (SEI), resulting in rapid decay of capacity.[1−3,6] Over the past decade a number of elegant strategies have emerged to address the various aspects of this multifaceted challenge. These strategies generally fall into four categories, including size reduction that facilitates release of mechanical strain,[7−9] hollow structures that leave room for silicon expansion,[10−13] binder engineering that improves connectivity of silicon particles,[14−17] and surface coating that reduces uncontrolled growth of solid electrolyte interphase.[14,15,18−22] However, it remains an unmet goal to harness Si's potential. Particularly, it is known that at high mass loadings the structural integrity and electrical interconnection become exceedingly difficult to maintain during electrochemical cycling.[10−17]

Here, we show for the first time that chemical tailoring of the nanostructure interface with atomic oxygen can substantially improve the electrochemical performance of silicon/carbon nanotube (CNT) composite electrodes. Due to the inherently weak adhesion between Si and the carbon lattice,[23,24] a persistent challenge for nanocomposites in general,[25] Si detaches from the conductors and agglomerates during repeated electrochemical cycling. By chemically tailoring CNTs with atomic oxygen, we found that the poor interface between Si and carbon is significantly improved. Owing to this robust interface, Si stays firmly immobilized on CNTs, effectively blocking the delamination and agglomeration (Figure 1). Both structural integrity and electrical connectivity are well maintained throughout the entire electrode, thereby offering superior electrochemical performance.

Our interfacial approach is enabled by a simple dry chemistry that applies UV−ozone (UVO) to CNT yarns with controlled porosity. We found that UVO produces atomic oxygen capable of functionalizing CNTs exclusive to the outer walls. This surface limiting feature is distinctly different from oxygen plasma, whose highly energetic ionic species are penetrative and destructive,[23] and oxidative wet chemistry.[26] A desired degree of surface functionalization of CNTs is achieved by simply tuning the exposure time of UVO. The exceptional control is

Received: November 5, 2014
Revised: December 12, 2014
Published: December 16, 2014

   dx.doi.org/10.1021/nl504242k | *Nano Lett.* 2015, 15, 703−708

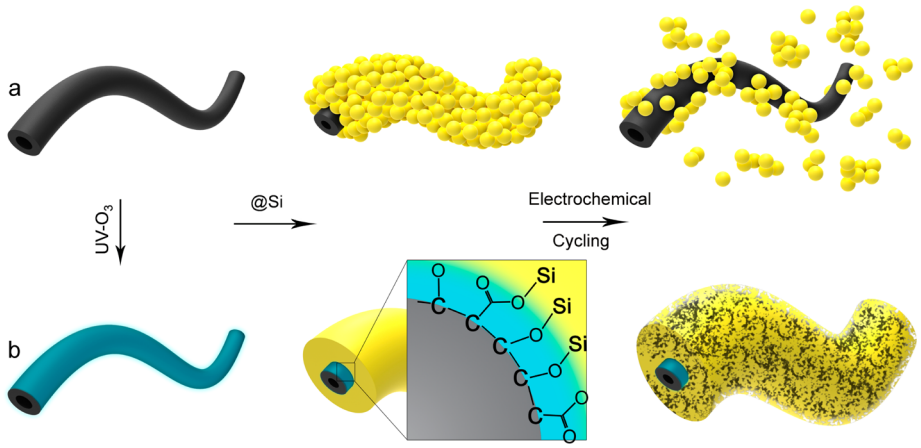

Figure 1. Schematic illustration of stabilizing Si anode by atomic oxygen-tailored interface. (a) Si grows on CNTs as particle aggregates, which detach from the conductive support during repeated electrochemical cycling. (b) Oxygen-containing moieties introduced by UV−ozone enable uniform nucleation of Si on CNTs. With robust interfacial bonding, Si adheres firmly on CNTs during electrochemical cycling.

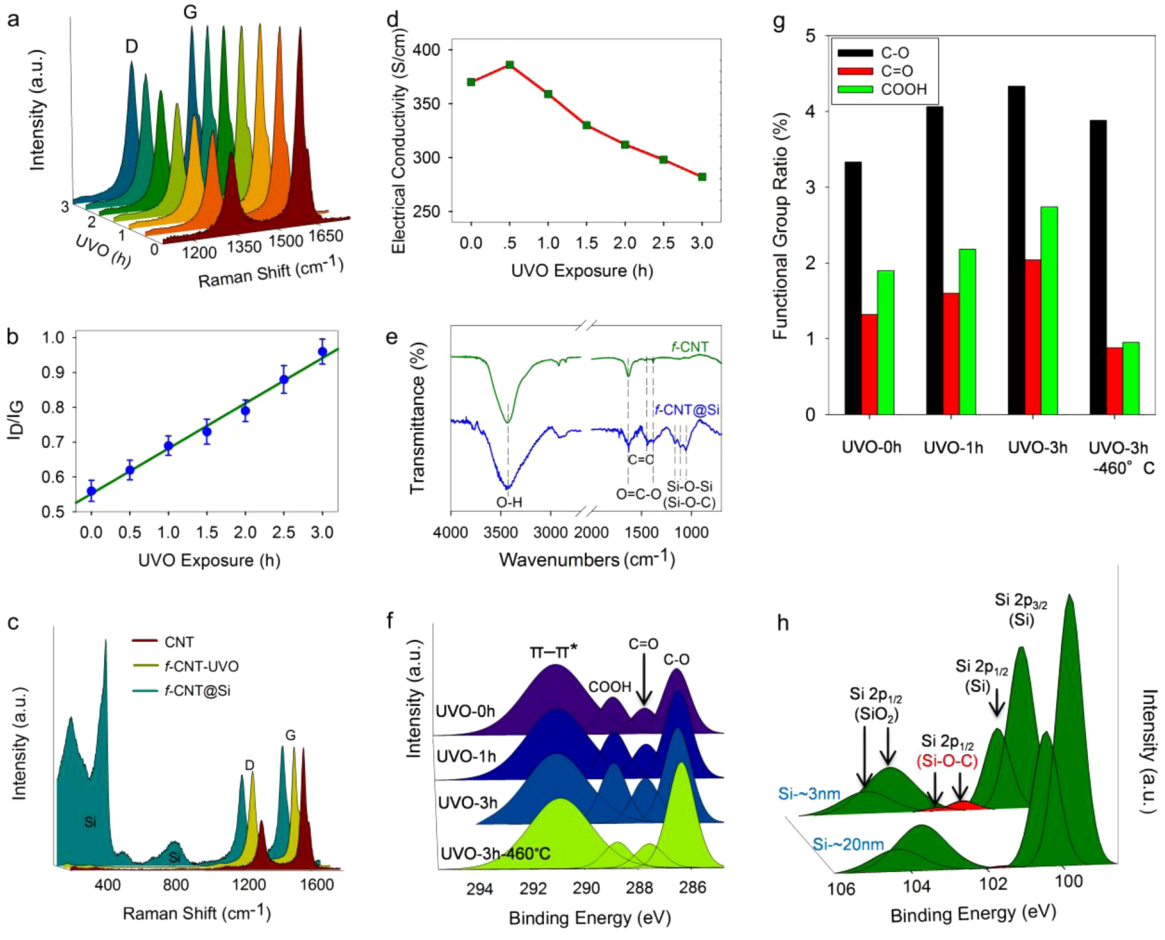

Figure 2. Experimental evidence of atomic oxygen-tailored Si/C interface. (a,b) Raman Spectra of CNTs with increasing time of UVO exposure. (c) Raman Spectra show a well-maintained defect density in *f*-CNT@Si. All Raman data are normalized by the intensity of the G band. (d) Electrical conductivity of a CNT yarn as a function of UVO exposure shows a 76% retention of conductivity after 3 h. (e) FT-IR spectra reveal the chemical nature of the functionalized structures. (f,g) C 1s XPS spectra show the density evolution of functional groups. For clarity, C—C peaks are not shown here. The peaks in panel f are normalized by the intensity of $\pi-\pi^*$ peak. The contents of all functional species increase with UVO exposure time. (h) Si 2p XPS spectra of *f*-CNTs with ~3 nm and ~20 nm of Si coating. The Si—O—C interfacial bonding is clearly evidenced.

evident by a linear increase in the integrated ratio of Raman D and G bands (I_D/I_G), which is a function of the defect density on the carbon lattice, as a function of the exposure time (Figure 2a,b). We note that there is typically a thin layer of amorphous carbon on the surface of multiwalled CNTs grown by chemical vapor deposition. Upon UVO exposure, most of the amorphous carbon was removed, as evident by high resolution transmission electron microscopy (HRTEM) (Supporting

dx.doi.org/10.1021/nl504242k | *Nano Lett.* 2015, 15, 703−708

Information Figure S1). Consistently, the electrical conductivity of the CNT yarn is slightly increased from 370 to 386 S/cm with 0.5 h UVO exposure (Figure 2d). The removal of the amorphous carbon, which weakly adheres on CNTs, exposes the nanotube surface for more effective functionalization.

Although further UVO treatment introduced chemical defects that eventually reduced the electrical conductivity of CNTs, a relatively high conductivity of 282 S/cm (76% retention) was preserved at a high defect density (I_D/I_G ~ 0.96), due to electrical percolation via intact inner tubes.[27] With Si coating, the conductivity remains high, at 259 S/cm, which is 7 orders of magnitude higher than Si (1.56×10^{-5} S/cm). The CNTs provide a conductive matrix that enables efficient electron transport and lithium ion diffusion within the entire electrode.[28,29] The high electrical conductivity makes it possible to eliminate the need of copper current collectors (~6 times heavier than CNTs) in order to further increase the energy density of batteries.

To quantify the interfacial bonding, we carried out Fourier transform infrared (FT-IR) spectroscopy and X-ray photoelectron spectroscopy (XPS) investigations. FT-IR spectra of the UVO functionalized CNTs (*f*-CNTs) confirm the existence of oxygen species, as evident by a broad absorption band at ~3435 cm^{-1} corresponding to O−H stretching mode, the peaks at ~1632 and 1385 cm^{-1} related to carboxylate (O═C—O) asymmetric and symmetric vibrations respectively,[16] and a peak at ~1466 cm^{-1} attributed to C═C stretching vibrations (Figure 2e). The growth of Si introduces a new triplet (1058−1165 cm^{-1}) that is comprised of Si—O—Si and Si—O—C stretching modes.[16] The surface density of the oxygen-containing functional species was further quantified by XPS. The oxygen content increased from 3.34 at. % to 4.05 at. % for 3 h of UVO exposure (Supporting Information Figure S3). We note that a large portion of oxygen species in the non-functionalized CNTs are derived from surface amorphous carbon which was mostly removed during the UVO exposure. Annealing of the *f*-CNTs at 460 °C under argon reduced the oxygen content from 4.05 at. % to 2.32 at. %, suggesting that some functional groups may decompose (or become reactive) during the Si growth.

The C 1s XPS spectra revealed three characteristic peaks of oxygen species corresponding to COOH (288.7 eV), C═O (287.3 eV), and C—O (C—O—C and C—OH) (286.3 eV) groups (Figure 2f, Supporting Information Figure S4).[30] The concentrations of all these functional species increase with UVO exposure (Figure 2f,g). Even annealed at 460 °C (the temperature for Si growth), *f*-CNTs retain a considerable amount of functional groups (3.81 at. % C—O, 0.68 at. % C═O, and 0.64 at. % COOH). We note that nearly all the oxygen species are on the outer-wall of a CNT due to the nature of UVO chemistry. Because XPS signals were collected from both outer-wall and some inner-walls due to its sampling depth (~6 nm for graphite at 1203 eV, NIST Standard Reference Database 71), the oxygen content on the outer-wall should be much higher than the XPS value. We estimated an oxygen content of 11.50 at. % on the outer-wall of *f*-CNTs (Supporting Information Figure S5).

The high surface density of oxygen groups enables robust interfacial bonding between Si and CNT. The formation of covalent Si—O—C interfacial bonding is unambiguously verified by XPS. Figure 2h depicts Si 2p XPS spectra of *f*-CNTs with ~3 nm Si coating. In addition to the characteristic peaks of Si (Si—Si, 99.8, 100.4 eV) and Si—O—Si from the outer SiO_x layer (103.7, 104.3 eV),[16] there are two bands at 101.3 and 101.9 eV that can be attributed to interfacial Si—O—C bonds. The interfacial origin of these XPS signatures is further confirmed by the absence of the Si—O—C signals when the *f*-CNTs were coated with ~20 nm Si, a thickness beyond the detection limit of XPS (<10 nm). Although XPS spectra reveal Si−O−C covalent bonding for *f*-CNT@Si, we note that *in situ* methods are necessary to fully elucidate the chemical nature and electrochemical evolution of the Si-carbon interface.

Besides the surface density, the spatial distribution of the functional groups is another important factor for the robustness and durability of the Si/C interface.[24] Under our experimental conditions, Si nucleates preferentially around the functional groups during low pressure chemical vapor deposition,[23,24] which provides a convenient experimental means to visualize the distribution and density of functional groups on the surface of CNTs. With the same deposition time, Si grew as nanoparticles on CNTs, but as a uniform coating (~15 nm) on *f*-CNTs (UVO-3 h) (Figure 3). The contents of Si were 38.3 and 40.8 wt % for CNT@Si and *f*-CNT@Si, respectively, with areal mass loadings of Si ~1.54 mg/cm^2 and ~1.71 mg/cm^2.

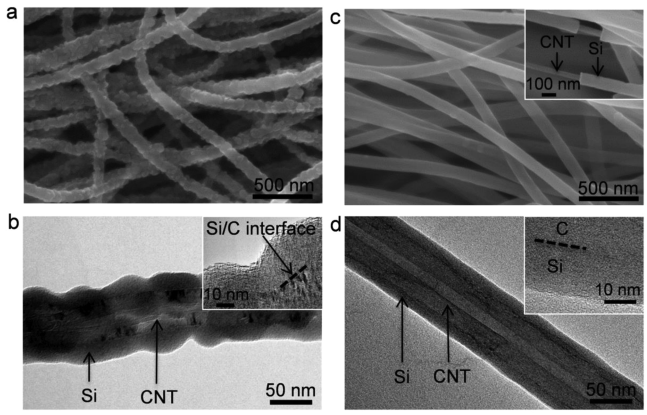

Figure 3. Functionalization controlled Si nucleation. (a) SEM and (b) TEM images show the growth of Si nanoparticles on pristine CNTs. (c) SEM and (d) TEM images reveal the growth of a conformable layer of Si on *f*-CNTs. Insets in (b−d) are SEM or HRTEM images with resolved CNT core, Si shell, and Si/C interface.

The chemically tailored Si/C interface significantly improved the electrochemical cycling performance. As shown in Figure 4a,b,c, at a lithiation/delithiation rate of C/5 (1C = 4.2 A per gram of Si, corresponding to 1.71 A per gram of entire electrode for *f*-CNT@Si), the reversible specific capacity of *f*-CNT@Si reached 869 mAh/g with an initial Coulombic efficiency (CE, the ratio of delithiation capacity to lithiation capacity) of 59.02% (Supporting Information Figure S8a). The CE quickly jumped to 92.3% at the second cycle and 98.7% after 10 cycles, which is favorably comparable to previous work on silicon based anodes.[11,15,17] The delithiation capacity is well retained, with 80% retention at the 100th cycle and 64% retention at the 160th cycle. In contrast, the first cycle delithiation capacity (843 mAh/g) of the nonfunctionalized control dropped to 677 mAh/g (80% retention) after 33 cycles and quickly decayed to 240 mAh/g (28.4% retention) after only 65 cycles. For the first cycle, the relatively low CE, a common phenomenon associated with Si anodes, derives from

dx.doi.org/10.1021/nl504242k | *Nano Lett.* 2015, 15, 703−708

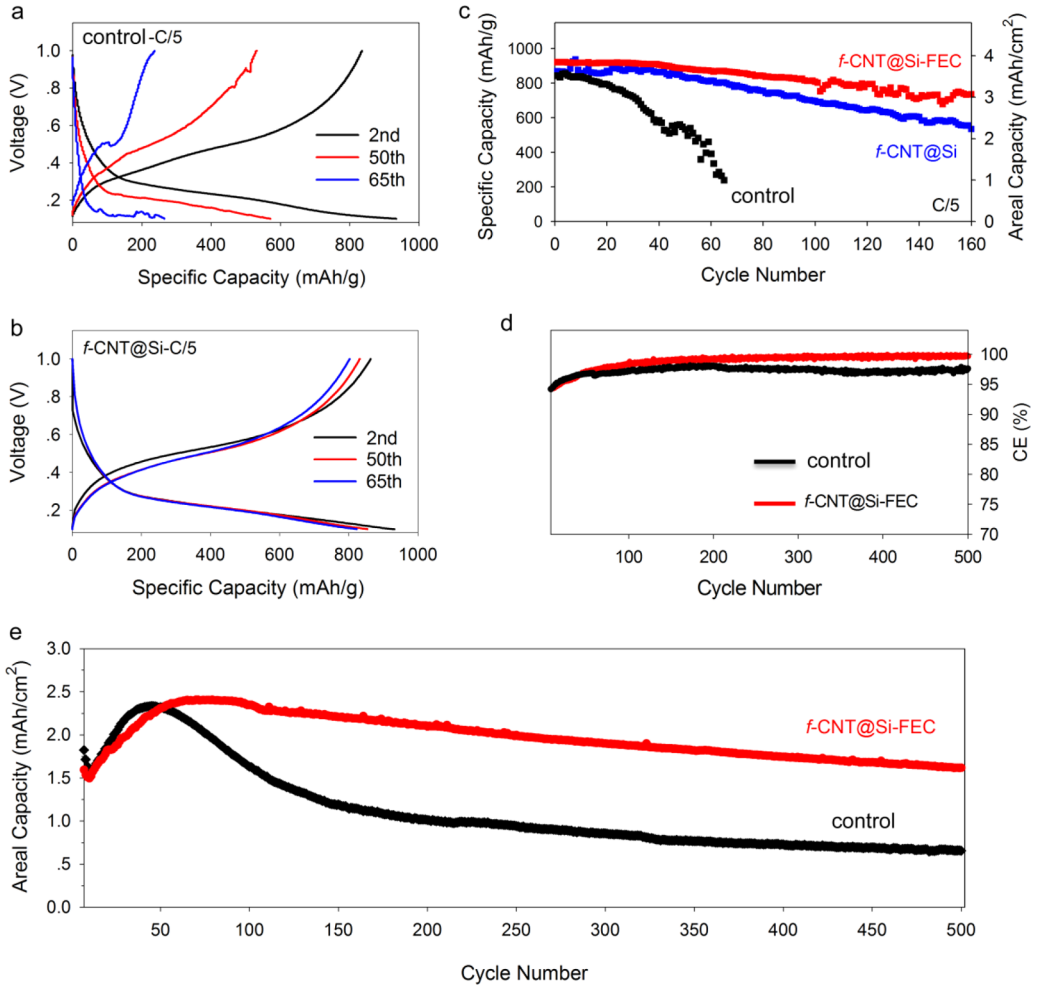

Figure 4. Improved electrochemical performance. (a,b) Voltage profiles at a lithiation/delithiation rate of C/5 (1C = 4.2 A per gram of Si). (c) Galvanostatic cycling performance of CNT@Si control and *f*-CNT@Si (left vertical axis) and delithiation areal capacity of *f*-CNT@Si (right vertical axis) at a rate of C/5. (d,e) Galvanostatic cycling performance of *f*-CNT@Si and control (Coulombic efficiency (d) and delithiation areal capacity (e)) at a rate of C/5 for the first through third cycles, C/2 for the fourth through sixth cycles, and 1C for all subsequent cycles (FEC electrolyte was used). For clarity, the first six cycles are not shown here but are provided in Supporting Information. All specific capacities were calculated based on the mass of the entire electrode.

the irreversible formation of SEI that consumes lithium and could be significantly improved by prelithiation.[12,19] Battery cycle life, which is defined as the number of complete lithiation/delithiation cycles before the battery capacity falls below 80% of its initial value, is an important parameter for evaluation of the cycling performance. With atomic oxygen tailored Si/C interface, the cycle life is improved by a factor of 3. The use of fluoroethylene carbonate (FEC) electrolytes in place of ethylene carbonate (EC) further improved the cycle life, achieving an accumulated improvement factor of nearly five (Figure 4c).

For the specific capacity, the interfacial tailoring enables a capacity of 922 mAh/g based on the mass of the entire electrode (Figure 4c), which is 4 times higher than the capacity of graphite electrode (229 mAh/g, based on the entire electrode with a mass ratio of graphite: carbon black: binder: Cu current collector = 8:1:1:2.98). The volumetric capacity is 737 mAh/cm^3, which is also higher than that of graphite anodes (600 mAh/cm^3).[5] This value can be further improved by reducing the CNT diameter and controlling the packing density of the CNT yarns. The areal capacity, another important parameter for batteries, is as high as 3.86 mAh/cm^2 (Figure 4c), which is among the highest of previously reported Si anodes.[11,19,21] Even after 160 cycles, the areal capacity is still above 3 mAh/cm^2 and a high retention of capacity (80%) was achieved with a tiny decay rate of 0.13%. We note that stable Si anodes with high areal capacities have rarely been reported; the only other work that we are aware of are pomegranate-like hollow particles[11] and nanosized Si embedded in mesoporous carbon.[19,21]

Even at a high lithiation/delithiation rate of 1C (4.2 A per gram of Si, corresponding to areal rates of 6.47 mA/cm^2 for CNT@Si and 7.18 mA/cm^2 for *f*-CNT@Si), a reversible areal capacity as high as 2.41 mAh/cm^2 was achieved for *f*-CNT@Si (Figure 4e). This high capacity at high rates can be attributed to the fast electron transport and efficient ion diffusion within the organized, conductive matrix composite.[28] Benefiting from the robust interfacial bonding, a superior cycling stability up to 500 cycles was achieved (1.62 mAh/cm^2 at the 500th cycle). The capacity retentions were 91.6% at the 150th cycle, 78.8% at the 300th cycle, and 67.1% at the 500th cycle. This superior cycling stability at a high mass loading of Si is among the highest reported.[11,21] In contrast, the capacity of the CNT@Si control quickly decayed to 1.2 mAh/cm^2 (51% retention) at the 150th

dx.doi.org/10.1021/nl504242k | *Nano Lett.* 2015, 15, 703−708

cycle and 0.66 mAh/cm^2 (28% retention) at the 500th cycle. The structural stability of *f*-CNT@Si is also manifested by an average Coulombic efficiency as high as 99.3% from 200 to 500 cycles, which is significantly higher than that of the CNT@Si control (97.0%) (Figure 4d). We note that the capacity increases during initial cycles, which is absent under a low lithiation rate (Figure 4c), as has also been previously observed on other Si based anodes and can be attributed to the delay of electrolyte wetting.[11,12,19]

It is known that the electrochemical cycling stability is strongly dependent on the loading density of active electrode materials (mass loading per unit volume).[1,11] At low loading densities, like those reported for sponge electrodes,[31] the detachment and aggregation of Si are not obvious; however, a highly packed electrode is desirable to achieve high volumetric energy density. To strike a balance between cycling stability and loading density of Si, we compared the electrochemical cycling performance of the Si-CNT composite electrodes with three different loading densities, including 0.51 g/cm^3, 0.78 g/cm^3, and 1.14 g/cm^3 of Si (Supporting Information Figure S9). The capacity retentions after 250 cycles are 82.9%, 63.5%, 26.5%, respectively. The optimal Si loading that maintains a good balance between cyclability and energy density falls in the range of 0.51−0.78 g/cm^3 for our system. At a loading density of 0.51 g/cm^3 Si, the *f*-CNT-Si yarns maintain high stability over 160 cycles. This high cyclability at high loading densities is made possible due to the interfacial bonding by oxygen, without which the capacity rapidly decays as shown by the controls.

To further elucidate the significant role of interfacial bonding to electrochemical cycling stability, we partially removed the functional groups by annealing *f*-CNTs at 800 °C under argon prior to Si growth. The high temperature annealing reduced the oxygen content to 1.13 at. %, less than 50% of that on *f*-CNTs annealed at 460 °C (2.32 at. %) (Supporting Information Figure S3). Raman scattering corroborates the partial loss of functional groups, with the I_D/I_G decreasing from 0.96 to 0.81. Despite the reduced surface density of oxygen-containing functional groups, a uniform Si coating was obtained. However, upon repeated electrochemical cycling, its capacity quickly decayed to 1.63 mAh/cm^2 (60% retention) at the 150th cycle, and 0.95 mAh/cm^2 (35% retention) at the 500th cycle (Supporting Information Figure S10). This cycling performance is still better than CNT@Si but evidently is much worse than *f*-CNT@Si.

We attribute the stable electrochemical cycling to the structural and electrical integrities of the *f*-CNT@Si matrix composite anode reinforced by the strong interfacial bonding. To observe the morphological changes of Si electrodes, after cycling testing, the electrodes were washed with acetonitrile followed by 0.5 M H_2SO_4 aqueous solution. For the CNT@Si control, Si was observed as aggregates of particles, segregating from the CNT matrix (Figure 5a). The structural failure can be attributed to the inherently weak interfacial adhesion between Si and carbon lattice. In stark contrast, Si remains immobilized on *f*-CNTs without delamination and agglomeration even after 500 cycles (Figure 5b,c). When more than 50% of the functional groups were removed by thermal annealing, the agglomeration of Si occurred (Supporting Information Figure S10), which coincides with the observed capacity decay. This control further illustrates the importance of robust interfacial bonding to stable cycling in Si anodes.

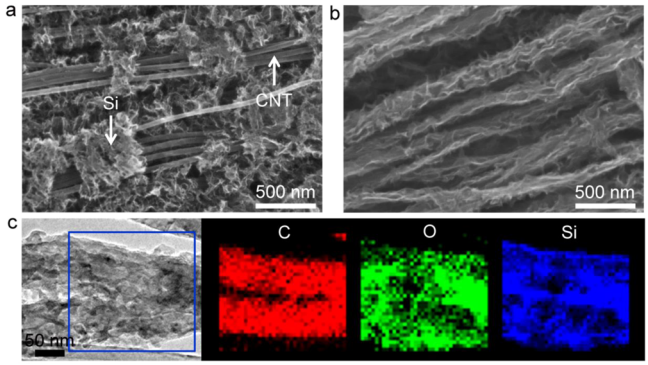

Figure 5. Evolution of electrode morphology. (a) Si detached from CNT surface and aggregated during electrochemical cycling. (b,c) In contrast, with atomic oxygen-tailored interface, Si is evidently immobilized on the surface of *f*-CNT even after 500 cycles, as confirmed by SEM and TEM elemental mapping.

■ ASSOCIATED CONTENT

Ⓢ Supporting Information

Figures S1−S10 and Tables S1 and S2 (Raman spectra, XPS, SEM and TEM images, and electrochemical performance) are included in the Supporting Information. This material is available free of charge via the Internet at http://pubs.acs.org.

■ AUTHOR INFORMATION

Corresponding Author

*E-mail: yhw@umd.edu.

Author Contributions

The manuscript was written through contributions of all authors. All authors have given approval to the final version of the manuscript.

Notes

The authors declare no competing financial interest.

■ ACKNOWLEDGMENTS

This work was initiated and supported as part of Nanostructures for Electrical Energy Storage (NEES), an Energy Frontier Research Center funded by the U.S. Department of Energy, Office of Science, Office of Basic Energy Sciences under Award Number DESC0001160. M.O. is partially supported by ARO contract W911NF-14-2-0024. We thank Jiaqi Dai for the creation of Figure 1, Dr. Kang Xu for providing the FEC electrolyte, Prof. Peter Kofinas for access to the microbalance, and Dr. Panju Shang for assistance with TEM.

■ REFERENCES

(1) Dunn, B.; Kamath, H.; Tarascon, J.-M. *Science* **2011**, *334*, 928−935.
(2) Choi, N.-S.; Chen, Z.; Freunberger, S. A.; Ji, X.; Sun, Y.-K.; Amine, K.; Yushin, G.; Nazar, L. F.; Cho, J.; Bruce, P. G. *Angew. Chem., Int. Ed.* **2012**, *51*, 9994−10024.
(3) Goodenough, J. B.; Park, K.-S. *J. Am. Chem. Soc.* **2013**, *135*, 1167−1176.
(4) Obrovac, M. N.; Christensen, L. *Electrochem. Solid-State Lett.* **2004**, *7*, A93−A96.
(5) Obrovac, M. N.; Christensen, L.; Le, D. B.; Dahnb, J. R. *J. Electrochem. Soc.* **2007**, *154*, A849−A855.
(6) Wu, H.; Cui, Y. *Nano Today* **2012**, *7*, 414−429.
(7) Chan, C. K.; Peng, H.; Liu, G.; McIlwrath, K.; Zhang, X. F.; Huggins, R. A.; Cui, Y. *Nat. Nanotechnol.* **2008**, *3*, 31−35.
(8) Magasinski, A.; Dixon, P.; Hertzberg, B.; Kvit, A.; Ayala, J.; Yushin, G. *Nat. Mater.* **2010**, *9*, 353−358.

(9) Liu, X. H.; Zhong, L.; Huang, S.; Mao, S. X.; Zhu, T.; Huang, J. Y. *ACS Nano* **2012**, *6*, 1522−1531.
(10) Hertzberg, B.; Alexeev, A.; Yushin, G. *J. Am. Chem. Soc.* **2010**, *132*, 8548−8549.
(11) Liu, N.; Lu, Z.; Zhao, J.; McDowell, M. T.; Lee, H.-W.; Zhao, W.; Cui, Y. *Nat. Nanotechnol.* **2014**, *9*, 187−192.
(12) Wu, H.; Chan, G.; Choi, J. W.; Ryu, I.; Yao, Y.; McDowell, M. T.; Lee, S. W.; Jackson, A.; Yang, Y.; Hu, L.; Cui, Y. *Nat. Nanotechnol.* **2012**, *7*, 310−315.
(13) Wang, B.; Li, X.; Zhang, X.; Luo, B.; Zhang, Y.; Zhi, L. *Adv. Mater.* **2013**, *25*, 3560−3565.
(14) Liu, G.; Xun, S.; Vukmirovic, N.; Song, X.; Olalde-Velasco, P.; Zheng, H.; Battaglia, V. S.; Wang, L.; Yang, W. *Adv. Mater.* **2011**, *23*, 4679−4683.
(15) Wang, C.; Wu, H.; Chen, Z.; McDowell, M. T.; Cui, Y.; Bao, Z. *Nat. Chem.* **2013**, *5*, 1042−1048.
(16) Kovalenko, I.; Zdyrko, B.; Magasinski, A.; Hertzberg, B.; Milicev, Z.; Burtovyy, R.; Luzinov, I.; Yushin, G. *Science* **2011**, *333*, 75−79.
(17) Ryou, M.-H.; Kim, J.; Lee, I.; Kim, S.; Jeong, Y. K.; Hong, S.; Ryu, J. H.; Kim, T.-S.; Park, J.-K.; Lee, H.; Choi, J. W. *Adv. Mater.* **2013**, *25*, 1571−1576.
(18) Luo, J.; Zhao, X.; Wu, J.; Jang, H. D.; Kung, H. H.; Huang, J. *J. Phys. Chem. Lett.* **2012**, *3*, 1824−1829.
(19) Li, X.; Gu, M.; Hu, S.; Kennard, R.; Yan, P.; Chen, X.; Wang, C.; Sailor, M. J.; Zhang, J.-G.; Liu, J. *Nat. Commun.* **2014**, *5*, 4105.
(20) Yi, R.; Dai, F.; Gordin, M. L.; Sohn, H.; Wang, D. *Adv. Energy Mater.* **2013**, *3*, 1507−1515.
(21) Zhang, R.; Du, Y.; Li, D.; Shen, D.; Yang, J.; Guo, Z.; Liu, H. K.; Elzatahry, A. A.; Zhao, D. *Adv. Mater.* **2014**, *26*, 6749−6755.
(22) Xiao, X.; Lu, P.; Ahn, D. *Adv. Mater.* **2011**, *23*, 3911−3915.
(23) Liao, H.; Karki, K.; Zhang, Y.; Cumings, J.; Wang, Y. *Adv. Mater.* **2011**, *23*, 4318−4322.
(24) Sun, C.-F.; Karki, K.; Jia, Z.; Liao, H.; Zhang, Y.; Li, T.; Qi, Y.; Cumings, J.; Rubloff, G. W.; Wang, Y. *ACS Nano* **2013**, *7*, 2717−2724.
(25) Ajayan, P. M.; Tour, J. M. *Nature* **2007**, *447*, 1066−1068.
(26) Brozena, A. H.; Moskowitz, J.; Shao, B.; Deng, S.; Liao, H.; Gaskell, K. J.; Wang, Y. *J. Am. Chem. Soc.* **2010**, *132*, 3932−3938.
(27) Piao, Y.; Chen, C.-F.; Green, A. A.; Kwon, H.; Hersam, M. C.; Lee, C. S.; Schatz, G. C.; Wang, Y. *J. Phys. Chem. Lett.* **2011**, *2*, 1577−1582.
(28) Sun, C.-F.; Zhu, H.; Baker, E. B., III; Okada, M.; Wan, J.; Ghemes, A.; Inoue, Y.; Hu, L.; Wang, Y. *Nano Energy* **2013**, *2*, 987−994.
(29) Chen, Z.; Yuan, Y.; Zhou, H.; Wang, X.; Gan, Z.; Wang, F.; Lu, Y. *Adv. Mater.* **2014**, *26*, 339−345.
(30) Wang, G.; Wang, H.; Lu, X.; Ling, Y.; Yu, M.; Zhai, T.; Tong, Y.; Li, Y. *Adv. Mater.* **2014**, *26*, 2676−2682.
(31) Hu, L.; Wu, H.; Gao, Y.; Cao, A.; Li, H.; McDough, J.; Xie, X.; Zhou, M.; Cui, Y. *Adv. Energy Mater.* **2011**, *1*, 523−527.